



# Control of TiO<sub>2</sub> electron transport layer properties to enhance perovskite photovoltaics performance and stability



Kun-Mu Lee<sup>a,b,c,d,\*</sup>, Wei-Jhih Lin<sup>a</sup>, Shih-Hsuan Chen<sup>a</sup>, Ming-Chung Wu<sup>a,b,c,d,\*\*</sup>

<sup>a</sup> Department of Chemical and Materials Engineering, Chang Gung University, Taoyuan, 33302, Taiwan

<sup>b</sup> Division of Neonatology, Department of Pediatrics, Chang Gung Memorial Hospital, Linkou, Taoyuan, 33305, Taiwan

<sup>c</sup> Green Technology Research Center, Chang Gung University, Taoyuan, 33302, Taiwan

<sup>d</sup> Center for Reliability Sciences and Technologies, Chang Gung University, Taoyuan, 33302, Taiwan

## ARTICLE INFO

### Keywords:

TiO<sub>2</sub>  
Electron transport layer  
Perovskite solar cell  
Photovoltaic  
Sub-module  
Hysteresis behavior

## ABSTRACT

This study demonstrates the effect of electron collection and transportation for TiO<sub>2</sub> electron transport layer (ETL) of the mesoscopic perovskite solar cells (PSCs). The influence of compact TiO<sub>2</sub> layer (c-TiO<sub>2</sub>) with various spray cycles, the particle size effect of mesoporous TiO<sub>2</sub> (meso-TiO<sub>2</sub>) film and post-treatment of TiO<sub>2</sub> electrode for perovskite solar cells have been studied systematically. We further optimize the meso-TiO<sub>2</sub> thickness to enhance the electron collection and transport efficiency and to reduce the anomalous J-V hysteresis phenomenon of PSCs. After adjusting the fabrication process of TiO<sub>2</sub> ETL, the highest performance of small cell PSC shows the power conversion efficiency (PCE) of 19.39% in the reverse scan and 19.12% in the forward scan, respectively. A sub-module PSC within an active area of 11.7 cm<sup>2</sup> exhibits impressive PCE of 16.03% under the illumination of 100 mW/cm<sup>2</sup> (AM1.5G). Moreover, it also shows an outstanding PCE of 25.49% under the illumination of 6000 lx of T5 indoor light source.

## 1. Introduction

Organic-inorganic based perovskite solar cells (PSCs) are considered to be the most competitive photovoltaic technology. Since Miyasaka group first reported CH<sub>3</sub>NH<sub>3</sub>PbX<sub>3</sub> perovskite sensitized solar cells which exhibited a power conversion efficiency (PCE) of 3.8%, the PCE of PSCs have been raised to over 24.2% in a decade [1–3]. Many researchers focus on the various chemistries of perovskite active layers, including doping, [4,5], substitution, [6–8], and interfacial engineering [9–11]. Our group adopted Ba<sup>2+</sup> in CH<sub>3</sub>NH<sub>3</sub>Pb<sub>1-x</sub>Ba<sub>x</sub>I<sub>3-y</sub>Cl<sub>y</sub> to partially replace lead cations, and it can be stably processed in the environment containing moisture and exhibits the PCE of 14.9% [4]. Kanatzidis group fabricated a perovskite material with 50% of Sn doping concentration (CH<sub>3</sub>NH<sub>3</sub>Sn<sub>0.5</sub>Pb<sub>0.5</sub>I<sub>3</sub>), which can efficiently regulate the bandgap of the perovskite material from 1.55 to 1.17 eV. Besides, CH<sub>3</sub>NH<sub>3</sub>Sn<sub>0.5</sub>Pb<sub>0.5</sub>I<sub>3</sub> shows superior film coverage and morphology, which ensures connectivity between grains and overcomes short-circuiting and charge leaking issues. This shows the broadest light absorption and highest short-circuit photocurrent density of ~20 mA/cm<sup>2</sup> [8]. For interfacial engineering, N. G. Park group reported a grain boundary healing process and achieved a PCE of 20.4% [12]. S. I. Seok

group showed a two-step process based on an intramolecular exchange between organic cations and DMSO molecules to fabricate FAPbI<sub>3</sub> based PSCs with exceeding 20% of PCE [13]. They further managed the content of iodide in perovskite film by addition of iodide ion in the fabrication process and thus decrease the deep-level defects and improve the PCE to 22.1% [14]. For the physical characteristics of perovskite active layers, many researchers also focus on studying the generation of electron and hole, carrier separation, recombination, and transportation. Therefore, a high-performance PSC consists of not only the composition and quality of perovskite layer, but also the properties of electron and hole transport layers [15–22] and interface engineering [23–26].

As a potential electron-transporting material, it should exhibit wide bandgap allowed more light to pass through to perovskite active layer, good electron mobility to facilitate electron collection, and proper band alignment with perovskite active layer to promote electron migrate to electron transport layer (ETL) and block the hole to pass through [27–29]. TiO<sub>2</sub>-based electron transport materials attract a lot of interest due to the proper electronic band levels and the ease of fabrication. TiO<sub>2</sub>-based ETL is preferred to facilitate interfacial charge transfer and to diminish charge carrier trapping and thus enhancing the PCE. Our

\* Corresponding author. Department of Chemical and Materials Engineering, Chang Gung University, Taoyuan, 33302, Taiwan.

\*\* Corresponding author. Department of Chemical and Materials Engineering, Chang Gung University, Taoyuan, 33302, Taiwan.

E-mail address: [kmlee@mail.cgu.edu.tw](mailto:kmlee@mail.cgu.edu.tw) (K.-M. Lee).

group used zinc-doped mesoscopic TiO<sub>2</sub> ETL to reach the optimal band alignment with perovskite and get an improved PCE of 18.3% [29]. The high-performance PSCs have been achieved with n-i-p mesoscopic device architecture, in which a compact TiO<sub>2</sub> (c-TiO<sub>2</sub>) layer and a mesoscopic TiO<sub>2</sub> (meso-TiO<sub>2</sub>) film play essential roles in charge collection, charge transport, and the scaffold for loading the high-quality perovskite active layer and also be seen as an excellent electron-hole separator [26,29–32]. This part needs to be systematically and clearly articulated.

Many methods have been used to prepare c-TiO<sub>2</sub> layer, including atomic layer deposition, [33,34], spin coating, [35], and spray pyrolysis [36,37]. For the spray pyrolysis method, it combines the processes, including nebulization, precipitation, pyrolysis, and sintering. Through these sequential and continuous processes, we can construct particles with homogeneous compositions and can precisely control the chemical composition during the solid-state reaction. Therefore, the spray pyrolysis method is commonly used to fabricate dense TiO<sub>2</sub> thin layer which exists fewer defects and shows efficient charge carrier transport property. The meso-TiO<sub>2</sub> film helps with electron injection and transport in PSCs. Meso-TiO<sub>2</sub> film helps the generated charge carriers in the perovskite active layer to be well separated and reduces the charge accumulation and electron-hole flux balance [38–40]. As well known, anatase TiO<sub>2</sub> were widely used in PSCs as electron transport materials. However, other phases of TiO<sub>2</sub> were also studied in PSCs and showed attractive results [41–43]. Furthermore, the charge injection from the perovskite layer to the TiO<sub>2</sub> layer can be enhanced by increasing the perovskite/meso-TiO<sub>2</sub> interfacial area, that is, the improvement of surface area of the meso-TiO<sub>2</sub>. Decreasing TiO<sub>2</sub> NP size is expected to be beneficial to the PSC photovoltaic performance. However, enlarging the surface area of TiO<sub>2</sub> NP does not always give an improvement in PCE, because electron transport and penetration of perovskite precursor solution into meso-TiO<sub>2</sub> film should be simultaneously considered [38–40]. Although the study on the size effect of TiO<sub>2</sub> NPs for ETL has previously published, it only focuses on fully printable mesoscopic PSC [44]. To obtain high performance PSCs, the size effect of TiO<sub>2</sub> for n-i-p type mesoscopic PSC should be studied thoroughly.

In this study, we systematically study the spray cycles of c-TiO<sub>2</sub>, TiO<sub>2</sub> NPs size, meso-TiO<sub>2</sub> film thickness and post-treatment of TiO<sub>2</sub> electrode to realize the charge injection and electron transport properties of the TiO<sub>2</sub> ETL. The correlations between the properties of ETL and PSC performance are studied and achieved excellent PCEs of 19.39% and 16.03% for small cell and sub-module PSCs, respectively. Moreover, improvement of J-V hysteresis behavior, PSC performance under dim light conditions, and short-term stability of device under thermal conditions are investigated in detail.

## 2. Experimental section

### 2.1. Preparation of TiO<sub>2</sub> nanoparticles of various sizes and TiO<sub>2</sub> paste

TiO<sub>2</sub> nanoparticles and TiO<sub>2</sub> paste preparation and the fabrication of electrode were carried out based on the studies reported previously with the exception of autoclave temperature variation [45,46]. Typical synthesis of TiO<sub>2</sub> nanoparticles (TiO<sub>2</sub> NPs) can be described as follows. At room temperature, 125 mL of titanium isopropoxide (97%) was added to 750 mL of 0.1 M nitric acid solution under vigorous stirring, and a white precipitate forms instantaneously. After the hydrolysis, the slurry was immediately heated to 80 °C then vigorously stirred for 12 h, and the peptization was achieved. To remove nonpeptized agglomerates, the solution was filtered on a glass frit. To adjust the final solids concentration to ~7.0 wt%, water was added to the filtrate. The reaction temperature and reaction time depend on the desired particle size. The growth of particles up to 15–36 nm was achieved under hydrothermal conditions in a titanium autoclave with various synthesis parameters. The reaction temperatures ranged from 160 °C to 240 °C, and the reaction time ranged from 12 to 24 h. During the autoclaving,

sedimentation occurred. In order to disperse the particles, a titanium ultrasonic horn was utilized. After the sonication process, the colloidal suspension was introduced by a rotary evaporator and consequently evaporated to a TiO<sub>2</sub> with a concentration of 15.0 wt%. The screen-printable TiO<sub>2</sub> pastes were homogeneously mixed with 4.23 g TiO<sub>2</sub> NP, 55 mL of ethyl cellulose, and 45 mL of terpineol. The thickness of TiO<sub>2</sub> film was measured by a profilometer (Sloan Dektak 3030). Pore diameter, pore volume and surface area of TiO<sub>2</sub> were measured by Brunauer–Emmett–Teller method (BET, Micrometrics Instruments ASAP 2020), utilizing accelerated porosimetry and surface area.

### 2.2. Preparation of perovskite solar cells

The perovskite solar cells preparation procedure flow chart is shown in Figure S1. By spraying titanium diisopropoxide bis(acetylacetonate) (75.0 wt% of Ti(AcAc)<sub>2</sub>OiPr<sub>2</sub> in isopropanol) solution at 450 °C, the TiO<sub>2</sub> compact layer was deposited onto the surface of FTO glass substrate. A mesoporous TiO<sub>2</sub> film with various particle sizes was screen printed onto the c-TiO<sub>2</sub>/FTO glass using TiO<sub>2</sub> pastes synthesized above and heated to 500 °C for 30 min and then put in TiCl<sub>4(aq)</sub> solution (0.3 M) at 70 °C for post treatment if need. Li-treated mesoporous TiO<sub>2</sub> film was accomplished by spin coating a 0.1 M solution of Li-TFSA in acetonitrile. The solution was prepared freshly before the application in nitrogen atmosphere. 200 μl were poured on meso-TiO<sub>2</sub>/c-TiO<sub>2</sub>/FTO glass. After 10 s of loading time, the spinning programme started with an acceleration of 1,000 rpm/s to a final speed of 3,000 rpm, the substrate was left spinning for 30 s. Both Li-treated and untreated TiO<sub>2</sub> electrodes were completed with a second calcination step at 450 °C for 30 min. After cooling down to room temperature, TiO<sub>2</sub> electrodes were transferred to a nitrogen-filled glove box (< 5.0 RH%). CH<sub>3</sub>NH<sub>3</sub>I (MAI) was synthesized by stirring 27.86 ml CH<sub>3</sub>NH<sub>2</sub> (40% in methanol, Aldrich) and 30 ml HI (57 wt% in water, Aldrich) in a 250 ml round-bottom flask at 0 °C for 4 h. The precipitate was recovered by evaporating at 55 °C for 1 h. The synthesized MAI was dissolved in ethanol, recrystallized in diethyl ether, and finally dried at 60 °C in a vacuum oven for 24 h. A mixed solution of PbI<sub>2</sub> (1.25 M) and MAI (1.25 M) dissolved in γ-butyrolactone (GBL) and DMSO (5/5, v/v) was coated onto the TiO<sub>2</sub> electrodes by a two-step spin-coating process at 1000 rpm for 10 s and then at 5000 rpm for 20 s. The perovskite films were treated with 50 μL toluene drop-casting in the second spin-coating step. The films were thermally treated on a hot plate at 100 °C for 10 min. For the corresponding hole-transporting material (HTM) solution from previous step, Spiro-OMeTAD was dissolved in chlorobenzene (50 mg/mL), 17.5 μL solution of lithium bis(trifluoromethane)sulfonimide (Li-TFSI, 520 mg) in 1.0 mL acetonitrile, and 28.5 μL 4-*tert*-butylpyridine (TBP) were added directly. The solution of as-prepared HTM was spin-coated onto the substrate glass of CH<sub>3</sub>NH<sub>3</sub>PbI<sub>3</sub>/meso-TiO<sub>2</sub>/c-TiO<sub>2</sub>/FTO at 2000 rpm for 30 s. Lastly, 100 nm of Ag cathode layer was thermally evaporated onto the substrate glass. The active area of small cell and sub-module (five cells in series on 5 cm × 5 cm substrate) were fixed at 0.16 cm<sup>2</sup> and 11.7 cm<sup>2</sup>, respectively. The schematic of sub-module PSC showed in Figure S1.

All samples were measured by a Hitachi UV–vis spectrophotometer (U-4100) to determine the UV–vis absorption spectra. With a Bruker powder diffractometer (D8 Discover) equipped with a 2D detector using CuKα1 radiation, GIXRD data were obtained in the 2-theta range of 10–50°. The scanning electron micrographs (SEM) were measured using a Hitachi S-800 microscope at 10.0 kV. An IPCE spectrometer (EQE-R-3011, ENLI Technology Co. Ltd., Taiwan) measured the incident monochromatic photon-to-current conversion efficiency (IPCE), and it was calibrated with a single-crystal silicon reference cell. The IPCE is calculated by equation:

$$\text{IPCE}(\%) = \text{LHE}(\lambda) \times \phi_{inj} \times \eta_c = 1240 \times \frac{I_{sc} \left( \frac{\text{A}}{\text{cm}^2} \right)}{\lambda(\text{nm}) \times P_{inc} \left( \frac{\text{W}}{\text{cm}^2} \right)} \times 100$$

The LHE( $\lambda$ ) where indicates the light harvesting efficiency,  $\phi_{inj}$  indicates the electron injection efficiency, and  $\eta_c$  indicates the charge collection efficiency.

A solar simulator (Yamashita Denso Corporation, YSS-50A) was utilized as the irradiation light source for the typical current density-voltage (J-V) measurements. The simulated AM 1.5G sunlight intensity was calibrated to 100 mW/cm<sup>2</sup>. By applying the potential external bias to the cell and measuring the photocurrent output with a Keithley model 2400 digital source meter (Keithley, USA), the cell J-V characteristics under illumination of AM 1.5G simulated sunlight were obtained. The J-V hysteresis index is calculated by the following equation [47]:

$$\text{Hysteresis index} = \frac{J_{RS}(0.8V_{OC}) - J_{FS}(0.8V_{OC})}{J_{RS}(0.8V_{OC})}$$

where  $J_{RS}(0.8V_{OC})$  and  $J_{FS}(0.8V_{OC})$  represent the photocurrent density at 80% of  $V_{oc}$  for the reverse scan (RS) and forward scan (FS), respectively.

For the dim light measurement, the cell J-V characteristics were measured by a Keithley model 2400 digital source meter, a Philips T5 fluorescent lamp illumination under 6500 K color temperature, and by changing the distance between light source and cells to control the light intensities. The scan direction was scanned from negative to positive bias. The irradiance and luminance were obtained by a NIST-traceable OPHIR radiometer (PD300-BB-50 mW) and a photometer (PD300-CIE), respectively.

### 3. Results and discussion

The compact TiO<sub>2</sub> layer (c-TiO<sub>2</sub>) of the electrode plays an essential role in the PSCs, which prevents the carrier from directly contacting the conductive glass substrate and the electron-hole recombination at the interface between the conductive glass and perovskite layer. PSC with perfect c-TiO<sub>2</sub> layer improves the open circuit voltage ( $V_{oc}$ ), fill factor (FF), and cell conversion efficiency. Therefore, we used spray pyrolysis method to prepare the c-TiO<sub>2</sub> layer on FTO glass by controlling the spray cycle number to increase the thickness of c-TiO<sub>2</sub> layer. Fig. 1 shows the SEM images of surface morphology of FTO and FTO/c-TiO<sub>2</sub> layers (cycle number: 1, 2, 5 and 10). The thin film grew with FTO surface crystal structure. Fig. 1 (f) shows a cross section view of compact and smooth c-TiO<sub>2</sub> layer on FTO with optimization of spray-2L condition. As the film got too thick (5L and 10L), the surface began to accumulate and produce some particles and resulted in the rough surface.

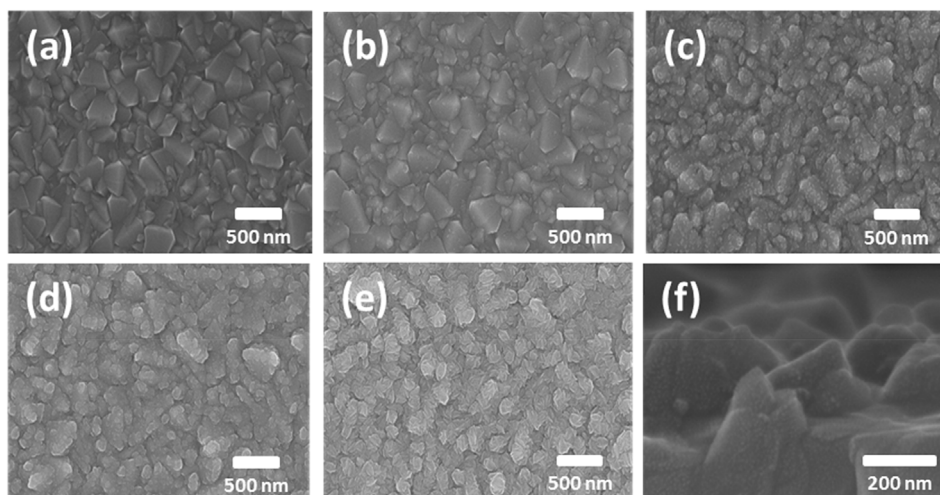


Fig. 1. The SEM top view images of c-TiO<sub>2</sub> by spray pyrolysis with various spray cycles: (a) FTO only; (b) 1 layer; (c) 2 layers; (d) 5 layers and (e) 10 layers. (f) The cross section view of spray-2L.

Fig. 2 (a) shows the cyclic voltammetry (CV) analysis, and the relationship between the spray layers and the cathodic peak current ( $i_{pc}$ ) value. The electrolyte medium for CV measurement of various c-TiO<sub>2</sub> films is in 0.5 mM K<sub>4</sub>Fe(CN)<sub>6</sub> and K<sub>3</sub>Fe(CN)<sub>6</sub> with 0.5 M KCl aqueous solution. The values were recorded at a scan rate of 50 mV/s. PSC efficiency is also illustrated in Fig. 2 (b). The  $i_{pc}$  value and the ratio of  $i_{pc}(c\text{-TiO}_2)/i_{pc}(\text{FTO only})$  are listed in Table S1. The  $i_{pc}$  obviously decreased when the FTO coated the c-TiO<sub>2</sub> layer and the spray-2L had a lowest  $i_{pc}$  value, which indicated the best-blocking effect on surface redox reaction. However, the  $i_{pc}$  increased again when spray cycle number increased up to 5L and 10L. This was due to the increase of surface area and could be explained by Randles-Sevcik equation, where the  $i_{pc}$  and surface area ( $A$ ) be proportional to each other.

For the device performance, we found that the PSC coated with 2L c-TiO<sub>2</sub> had the best performance and the smallest hysteresis index (HI), but the HI values increased when spraying cycle number increased to 5L and 10L. The reason is that the increased spray cycle numbers cause the increase of c-TiO<sub>2</sub> layer thickness. It increased the series resistance of the device, and the flower-like interface (spray-5L and 10L) may increase the probability of electron-hole recombination and charge accumulation at the interface, and resulting in the reduce of FF and  $V_{oc}$  and higher HI value (A device without hysteresis presents a HI of zero, while a higher value of HI indicates a more pronounced hysteresis.). Therefore, PSC with spray-2L c-TiO<sub>2</sub> layer showed the high power conversion efficiency at 16.93%.

Furthermore, the meso-TiO<sub>2</sub> film can provide a mesoporous framework to facilitate percolation of the perovskite solution, which can significantly increase the contact area between the perovskite material and the electron transport layer (ETL), and can effectively collect and inject the electron into ETL [40]. Therefore, four kinds of meso-TiO<sub>2</sub> films with thickness of 100, 150, 300 and 500 nm (as shown in Figure S2) and four kinds of TiO<sub>2</sub> NPs size of 22, 25, 30 and 36 nm were prepared, respectively, to investigate the effects of the interfaces on photovoltaic performance of PSCs.

Figure S3 shows the steady-state PL spectra of the perovskite film deposited on the lone c-TiO<sub>2</sub> film and c-TiO<sub>2</sub>/meso-TiO<sub>2</sub> film with various thicknesses. It appeared that the meso-TiO<sub>2</sub>/perovskite samples exhibited more evident PL quenching compared to the lone c-TiO<sub>2</sub> film/perovskite sample, which demonstrated more effective electron extraction at meso-TiO<sub>2</sub>/perovskite interface. The samples with 100 nm, 150 nm and 300 nm meso-TiO<sub>2</sub> films showed the similar PL intensities. Further, we found that the PSC with 150 nm meso-TiO<sub>2</sub> film had the best conversion efficiency of 17.81% for the reversed scan and 16.49% for the forward scan with an HI value of 0.054 (as shown in Figure S4

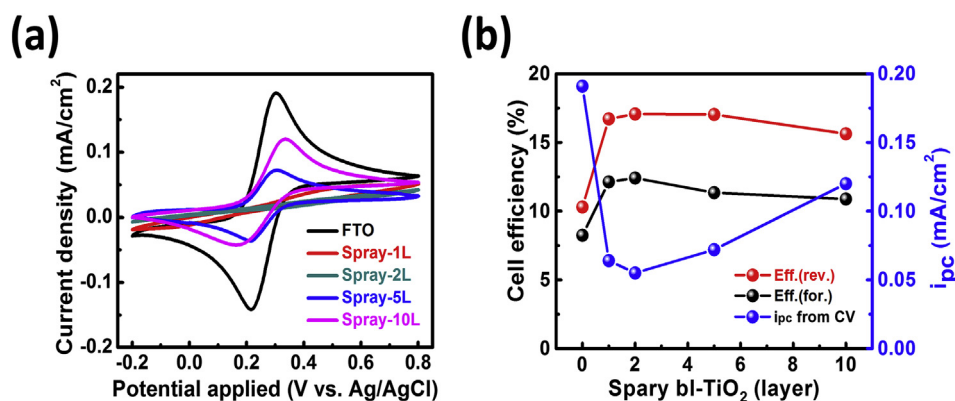


Fig. 2. (a) The CV measurement of c-TiO<sub>2</sub> films with various spray cycles. (b) The relationship between spray c-TiO<sub>2</sub> layer and cell performance.

and Table S3). The main reason was that when the meso-TiO<sub>2</sub> film got too thick (such as 500 nm), it lead to an increase in the series resistance (the increased area of TiO<sub>2</sub>/TiO<sub>2</sub> interface), which lead to a longer charge transport length. The thicker meso-TiO<sub>2</sub> film also made the perovskite precursor ineffective to penetrate and to deposit into the mesoporous film (generate vacancies in the meso-TiO<sub>2</sub> film). Those mainly influenced the PSC performance. After optimizing the above conditions, the charge injection from the perovskite to the TiO<sub>2</sub> layer could be further improved by increasing the perovskite/meso-TiO<sub>2</sub> interfacial area. The surface area of the TiO<sub>2</sub> NPs is expected to be beneficial to the PSC performance. To investigate the effect of the particle size of meso-TiO<sub>2</sub> on the photovoltaic properties, we fabricated four c-TiO<sub>2</sub>/150 nm meso-TiO<sub>2</sub> PSCs containing the above mentioned sized TiO<sub>2</sub> NPs to investigate the effects on the interfaces such as perovskite/TiO<sub>2</sub> or TiO<sub>2</sub>/TiO<sub>2</sub> on photovoltaic performance.

As for the TiO<sub>2</sub> particle size effect, Fig. 3 shows the SEM images of those 4 kinds of TiO<sub>2</sub> NPs. The mean diameters measured from the SEM images were 22.6, 25.0, 30.2 and 37.6 nm. The XRD patterns (Figure S5) confirms the meso-TiO<sub>2</sub> film containing anatase-phase TiO<sub>2</sub> NPs (JCPDS card no. 21–1272) from the main peak of the XRD pattern ( $2\theta = 25.281^\circ$ ) which corresponds to the (101) plane. Moreover, the

Table 1

BET surface area, pore volume and pore diameter of meso-TiO<sub>2</sub> films with various TiO<sub>2</sub> NPs.

TiO <sub>2</sub> particle size (nm)	S <sub>BET</sub> (m <sup>2</sup> /g)	Pore volume (cm <sup>3</sup> /g)		Pore diameter (nm)	
		BJH Adsorption	BJH Desorption	BJH Adsorption	BJH Desorption
22	86.23	0.353	0.351	13.53	12.19
25	85.11	0.383	0.386	14.93	13.59
30	67.86	0.479	0.478	23.99	22.06
36	55.35	0.504	0.503	30.75	27.97

structural characteristics of TiO<sub>2</sub> film such as BET surface area, total pore volume, and mean pore size of each film with various sizes of TiO<sub>2</sub> NPs are summarized in Table 1. The pore diameter of 13.5–30.8 nm, the pore volume of 0.35–0.50 cm<sup>3</sup>/g, and the surface area of 86.2 to 55.4 m<sup>2</sup>/g can be successfully tuned by controlling the size of TiO<sub>2</sub> NPs. The UV–vis of TiO<sub>2</sub> film and TiO<sub>2</sub>/perovskite films are shown in Figure S6. The absorbance of c-TiO<sub>2</sub>/meso-TiO<sub>2</sub> PSCs with various TiO<sub>2</sub> NPs shows little difference, which means that the perovskite films are not affected by the TiO<sub>2</sub> particles and pore size in the meso-TiO<sub>2</sub> film.

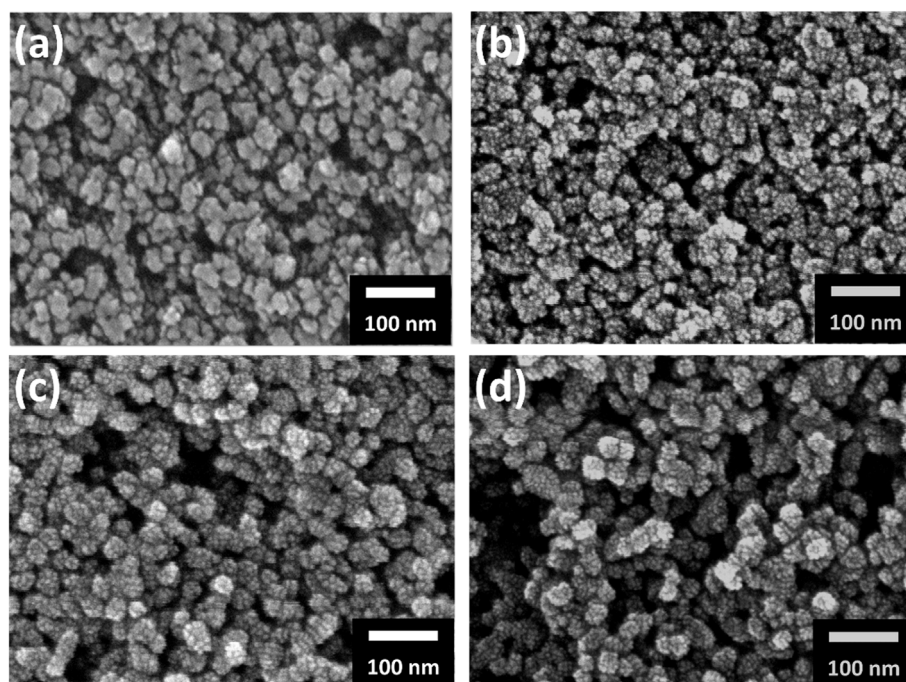


Fig. 3. Surface microstructure of meso-TiO<sub>2</sub> films with various TiO<sub>2</sub> NPs of (a) 22 nm; (b) 25 nm; (c) 30 nm and (d) 36 nm.

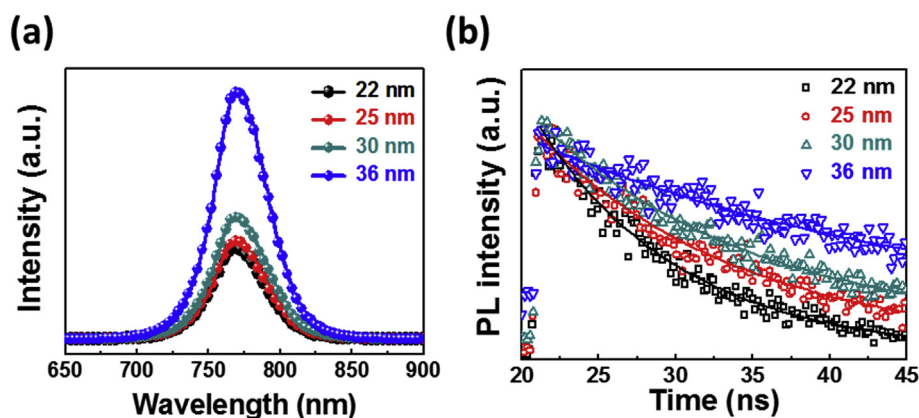


Fig. 4. (a) PL spectra and (b) TRPL spectra of perovskite/meso-TiO<sub>2</sub> films with various TiO<sub>2</sub> NP sizes.

Therefore, the changes in photoelectric properties are also not influenced by the perovskite film thickness.

Furthermore, to investigate the electron transport behavior and the carrier lifetime, the PL measurements of the perovskite films were investigated. Fig. 4 shows the charge injection and recombination properties of the prepared meso-TiO<sub>2</sub>/perovskite film substrates with various NPs sizes were evaluated using steady-state PL and TRPL. It appeared (Fig. 4 (a)) that the meso-TiO<sub>2</sub> film with smaller NPs exhibited more evident PL quenching compared to the ones with larger NP size. This meant more effective electron extraction with larger contact area at TiO<sub>2</sub>/perovskite interface. This can be mainly attributed to the fully penetration of perovskite precursor solution in meso-TiO<sub>2</sub> film and increased interface area. The TRPL spectra of all samples collected at 768 nm after excitation with a 532 nm laser and presented in Fig. 4 (b). The TRPL decay plots can be fitted by a bi-exponential decay function shown as below:

$$F(t) = A_1 \exp\left(-\frac{t}{\tau_1}\right) + A_2 \exp\left(-\frac{t}{\tau_2}\right)$$

where  $A_1$  and  $A_2$  represent time independent coefficient of amplitude fraction,  $\tau_1$  is fast decay time and  $\tau_2$  is slow decay time [48]. The average decay time ( $\tau_{ave}$ ) was calculated using the following equation:

$$\tau_{avg} = \frac{\sum_i A_i \tau_i}{\sum_i A_i}$$

When the perovskite film was deposited directly on the lone c-TiO<sub>2</sub> (c-TiO<sub>2</sub>/perovskite film), its average PL decay time ( $\tau_{ave}$ ) was 64.65 ns. For the c-TiO<sub>2</sub>/meso-TiO<sub>2</sub>/perovskite samples, the  $\tau_{ave}$  dropped to 9.96 ns for 22 nm NPs, 13.32 ns for 25 nm NPs, 15.02 ns for 30 nm NPs, and 31.00 ns for 36 nm NPs. For comparison purpose, the  $\tau_{ave}$  for the meso-TiO<sub>2</sub> with the commercial TiO<sub>2</sub> P25 (particle size ~30 nm) is 39.39 ns, due to P25 TiO<sub>2</sub> containing ~20% Rutile phase and has a lower electron transport behavior [49]. This confirms that the electron extraction is faster from the perovskite into the TiO<sub>2</sub> ETL when the meso-TiO<sub>2</sub> pair with a high ratio anatase and smaller TiO<sub>2</sub> particle. This is beneficial to the effective charge separation at the perovskite/ETL interface and more balance between electron and hole transport in device, resulting in a higher FF and  $V_{oc}$  and a lower HI value. The effect of Li-doping on the meso-TiO<sub>2</sub> films in the PSCs was also investigated.

Fig. 5 shows the size effects of meso-TiO<sub>2</sub> film (including Li-treated or not) on photovoltaic parameters of PSC. It was found that the FF and  $V_{oc}$  values of PSC increased with decreasing TiO<sub>2</sub> particle size, and the PSCs with Li-treated TiO<sub>2</sub> showed the higher cell performance and lower hysteresis behavior. The reason is that the Li-treated can improve the conductivity of meso-TiO<sub>2</sub> film, and it has been confirmed by the previous report [50]. The PSCs with smaller TiO<sub>2</sub> NP sizes (22 nm and 25 nm) showed apparent improvement in FF and PCE, especially when using Li-treated meso-TiO<sub>2</sub> film. Moreover, we have also investigated

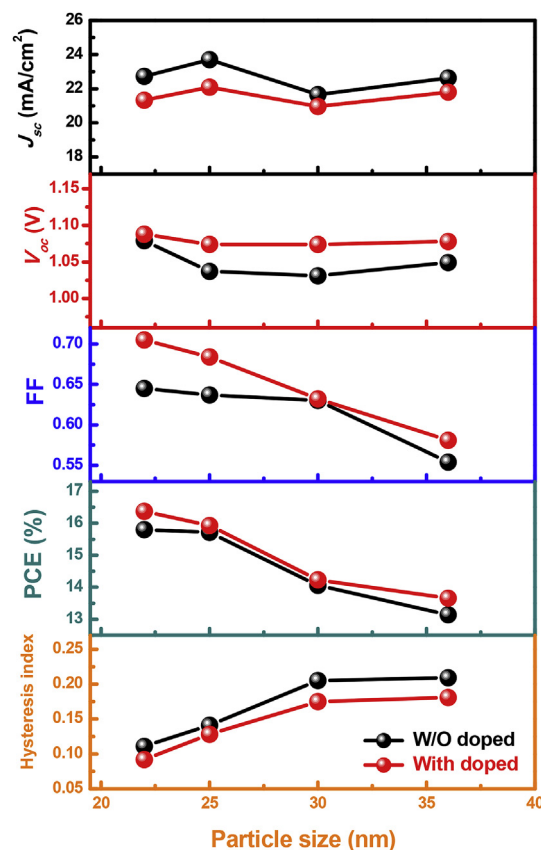


Fig. 5. The relationship between photovoltaic parameters of perovskite solar cell and TiO<sub>2</sub> nanoparticle size (with and without Li-treated meso-TiO<sub>2</sub> film).

the size effect in the meso-TiO<sub>2</sub> film for the perovskite film prepared by the blade coating process for reference (Table S4). We found that perovskite films prepared by spin cast and blade cast processes have similar tendency results, which the PSC with smaller TiO<sub>2</sub> NP in meso-TiO<sub>2</sub> film shows a better cell performance.

Owing to the hysteresis behavior being a significant issue in accurately characterizing the device efficiency, the steady-state photocurrent and PCE output at the maximum power point should be measured to gain the precise efficiency of the PSC [51]. Here, the on/off step photocurrent output of the PSCs with various sizes of TiO<sub>2</sub> NP ETLs are measured under one sun light illumination (100 mW/cm<sup>2</sup>) and gives a constant bias of  $V_{max}$  for over 300 s. As shown in Fig. 6, the photocurrent output rose to the maximum current value and the time to steady-state varied with NPs sizes. The on/off step test photocurrent

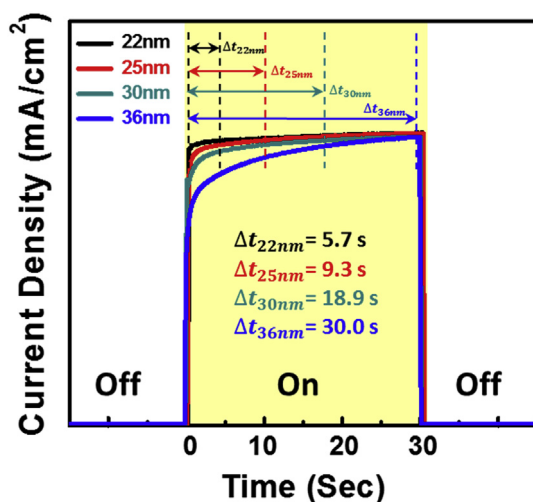


Fig. 6. J-t plot of on/off step light measurement for PSCs with various TiO<sub>2</sub> NP sizes to understand the time required to reach stable.

output of all devices were highly stable. The PSCs with smaller sized TiO<sub>2</sub> NPs, such as 22 and 25 nm, had a higher stable current and needed shorter time to reach the stable current ( $< 10$  s). For PSCs with larger sized TiO<sub>2</sub> NPs, such as 36 nm, had a lower stable current and needed longer time of more than 30 s to reach the stable current. This evidences the smaller particle size has better electron extraction efficiency, thus results in a less J-V hysteresis behavior. It works in correspondence with the above analysis results.

In order to further improve the TiO<sub>2</sub>-TiO<sub>2</sub> connection in meso-TiO<sub>2</sub> film, the meso-TiO<sub>2</sub> ETL was put into TiCl<sub>4</sub> (aq) at 70 °C for post-treatment process and the effect on PSC performance is illustrated in Figure S9. Post-treatment for 30 min had a better PSC performance (improve the conversion efficiency from  $\sim 16\%$  to  $> 18\%$ ), but the performance decreased when the post-treatment went on for longer time. It was due to too much TiO<sub>x</sub> forming in meso-TiO<sub>2</sub> film and reduced the pore size. This created difficulty in penetrating the CH<sub>3</sub>NH<sub>3</sub>PbI<sub>3</sub> precursor solution and in formatting some voids in the meso-TiO<sub>2</sub> film. Fig. 7(a) shows that after optimizing the fabrication process of TiO<sub>2</sub> ETL, the champion PSC device had a PCE of 19.39% for the reverse scan and 19.16% for the forward scan under the illumination of 100 mW/cm<sup>2</sup> (AM 1.5G).

The optimal TiO<sub>2</sub> ETL for PSC has been well investigated in the above. Here we demonstrate a sub-module PSC that constructed from a series connection of five cells (substrate area: 25 cm<sup>2</sup> and active area: 11.70 cm<sup>2</sup>). The J-V curve and photograph of the sub-module PSC is shown in Fig. 7(b). The CO<sub>2</sub>-laser patterning FTO process was adopted to fabricate an effective and integrated series connection between the

cells in the sub-module. the J<sub>SC</sub>, V<sub>OC</sub>, FF and PCE of 4.14 mA/cm<sup>2</sup>, 5.21 V, 0.743 and 16.03%, respectively, were achieved under 1 sun illumination. The PCE of the sub-module PSC shows more than 16% which is related to the well control and uniformity of each layers preparation in this perovskite solar sub-module.

Furthermore, we also measured the performance of PSCs under low light intensity of T5 light source. The PCE were higher than 20% under the illumination intensity of 1000–6000 lx, and showed the excellent PCE of 25.49% under 6000 lx (as shown in Figure S10). The PSC showed a better cell performance under the T5 fluorescent light source than that under a solar simulator because the T5 fluorescent light illuminates wavelength ranging from 350 to 750 nm (1.65 eV) and the spectral response of the CH<sub>3</sub>NH<sub>3</sub>PbI<sub>3</sub> in this study nicely covers this entire spectra. Moreover, we also put the performance of dye-sensitized solar cell (DSSC) for reference. The performances of PSC are better than that of DSSC under both the T5 light source and the solar simulator, which means that PSC has a better light-harvesting and light-to-electron conversion property under dim light conditions. With the low-cost solution process, such PSCs can be easily regarded as one of the most promising candidates for indoor or dim light energy harvesting.

Finally, the stability of PSC devices under a dark continual thermal environment of 60 and 80 °C was investigated. As observed in Fig. 8, the V<sub>OC</sub> was slightly improved within the first 100 min for both 60 and 80 °C conditions, which was due to the energy band alignment at the interface of TiO<sub>2</sub>/CH<sub>3</sub>NH<sub>3</sub>PbI<sub>3</sub> or CH<sub>3</sub>NH<sub>3</sub>PbI<sub>3</sub>/HTM. The device efficiency decreased only from  $\sim 17\%$  to 15% and 13% at 60 and 80 °C, respectively, without having any device encapsulations after an 1100 min test. The major decrease of PSC performance at 80 °C was the decline of FF in the first 200 min. This might be the result of not well-matched thermal expansion coefficient of layers or the extrinsic factors (e.g., H<sub>2</sub>O and O<sub>2</sub>) [52] that resulted in the escaping of CH<sub>3</sub>NH<sub>3</sub>I in CH<sub>3</sub>NH<sub>3</sub>PbI<sub>3</sub> and additives in HTM of device under higher temperature condition.

#### 4. Conclusions

In this study, a hole blocking compact TiO<sub>2</sub> layer (c-TiO<sub>2</sub>) was prepared by spray pyrolysis method, and screen printed meso-TiO<sub>2</sub> layers with various TiO<sub>2</sub> particle sizes were hydrothermally synthesized to prepare an optimal mesoporous TiO<sub>2</sub> layer which was used as an electron transport layer of the n-i-p type perovskite solar cell. The use of spray pyrolysis to prepare a high quality c-TiO<sub>2</sub> layer not only improved the electron collection and transportation in the TiO<sub>2</sub> film, but also prevented directly contact between the hole/carrier and the conductive FTO glass. This effectively increased the V<sub>OC</sub> and FF of PSC. The 2L c-TiO<sub>2</sub> and 150 nm meso-TiO<sub>2</sub> film with 22 nm NPs showed the best properties of electrons injection into the ETL, which effectively improving the J<sub>SC</sub>, V<sub>OC</sub> and FF of the PSC and the J-V hysteresis behavior.

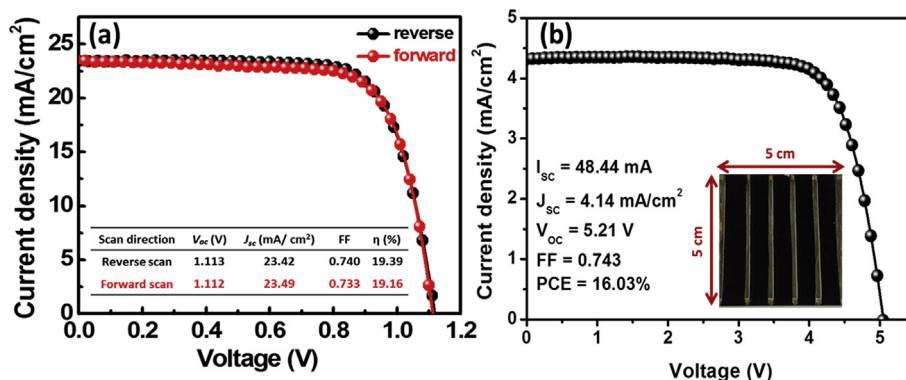


Fig. 7. The J-V curve and efficiency of (a) the champion PSC (active area = 0.16 cm<sup>2</sup>) and (b) sub-module PSC (active area = 11.7 cm<sup>2</sup>) measured under illumination of 100 mW/cm<sup>2</sup>, AM1.5G.

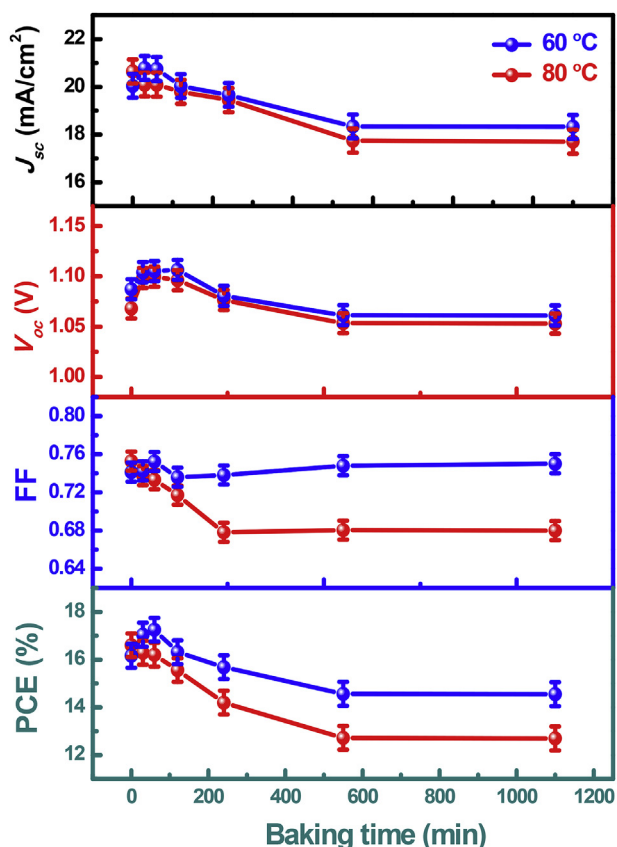


Fig. 8. The thermal stability of PSCs under 60 and 80 °C in dark.

After optimizing the fabrication process of TiO<sub>2</sub> ETL, the PSCs achieved excellent PCEs of 19.39% and 16.03% for small cell and sub-module PSCs, respectively, under the illumination of 100 mW/cm<sup>2</sup> (AM 1.5G) and showed even better PCE of 25.49% under the illumination of 6000 lx of T5 light source.

#### Acknowledgments

This work was supported by Ministry of Science and Technology, Taiwan (MOST 108-2628-E-182-003-MY3 and MOST 106-2221-E-182-057-MY3); Chang Gung University (QZRPD181) and Chang Gung Memorial Hospital, Linkou (CMRPD2G0302, BMRPF67 and BMRPC74).

#### Appendix A. Supplementary data

Supplementary data to this article can be found online at <https://doi.org/10.1016/j.orgel.2019.105406>.

#### References

- J.-P. Correa-Baena, M. Saliba, T. Buonassisi, M. Grätzel, A. Abate, W. Tress, A. Hagfeldt, Promises and challenges of perovskite solar cells, *Science* 358 (2017) 739–744.
- <https://www.nrel.gov/pv/assets/pdfs/pv-efficiency-chart.20190103.pdf>.
- S.F. Völker, S. Collavini, J.L. Delgado, Organic Charge Carriers for Perovskite Solar Cells 8 (2015) 3012–3028.
- S.-H. Chan, M.-C. Wu, K.-M. Lee, W.-C. Chen, T.-H. Lin, W.-F. Su, Enhancing perovskite solar cell performance and stability by doping barium in methylammonium lead halide, *J. Mater. Chem.* 5 (2017) 18044–18052.
- S. Gharibzadeh, F. Valduga de Almeida Camargo, C. Roldán-Carmona, G.C. Gschwend, J. Pascual, R. Tena-Zaera, G. Cerullo, G. Grancini, M.K. Nazeeruddin, Picosecond capture of photoexcited electrons improves photo-voltaic conversion in MAPbI<sub>3</sub>:C70-doped planar and mesoporous, *Sol. Cells* 30 (2018) 1801496.
- Z. Li, C. Kolodziej, C. McCleese, L. Wang, A. Kovalsky, A.C. Samia, Y. Zhao, C. Burda, Effect of chloride substitution on interfacial charge transfer processes in MAPbI<sub>3</sub> perovskite thin film solar cells: planar versus mesoporous, *Nanoscale Adv.* 1 (2019) 827–833.
- F. Li, Z. Xia, C. Pan, Y. Gong, L. Gu, Q. Liu, J.Z. Zhang, High Br<sup>-</sup> content CsPb (ClyBr<sub>1-y</sub>)<sub>3</sub> perovskite nanocrystals with strong Mn<sup>2+</sup> emission through diverse cation/anion exchange engineering, *ACS Appl. Mater. Interfaces* 10 (2018) 11739–11746.
- F. Hao, C.C. Stoumpos, R.P.H. Chang, M.G. Kanatzidis, Anomalous band gap behavior in mixed Sn and Pb perovskites enables broadening of absorption spectrum in solar cells, *J. Am. Chem. Soc.* 136 (2014) 8094–8099.
- Y. Bai, X. Meng, S. Yang, *Interface Engineering for Highly Efficient and Stable Planar P-I-N Perovskite Solar Cells* vol. 8, (2018), p. 1701883.
- H. Wang, F. Cai, M. Zhang, P. Wang, J. Yao, R.S. Gurney, F. Li, D. Liu, T. Wang, Halogen-substituted fullerene derivatives for interface engineering of perovskite solar cells, *J. Mater. Chem.* 6 (2018) 21368–21378.
- A.-N. Cho, N.-G. Park, *Impact of Interfacial Layers in Perovskite Solar Cells* vol. 10, (2017), pp. 3687–3704.
- D.-Y. Son, J.-W. Lee, Y.J. Choi, I.-H. Jang, S. Lee, P.J. Yoo, H. Shin, N. Ahn, M. Choi, D. Kim, N.-G. Park, Self-formed grain boundary healing layer for highly efficient CH<sub>3</sub>NH<sub>3</sub>PbI<sub>3</sub> perovskite solar cells, *Nature Energy* 1 (2016) 16081.
- W.S. Yang, J.H. Noh, N.J. Jeon, Y.C. Kim, S. Ryu, J. Seo, S.I. Seok, High-performance photovoltaic perovskite layers fabricated through intramolecular exchange, *Science* 348 (2015) 1234–1237.
- W.S. Yang, B.-W. Park, E.H. Jung, N.J. Jeon, Y.C. Kim, D.U. Lee, S.S. Shin, J. Seo, E.K. Kim, J.H. Noh, S.I. Seok, Iodide management in formamidinium-lead-halide-based perovskite layers for efficient solar cells, *Science* 356 (2017) 1376–1379.
- C.L. David, D.L. Kevin, B.T. Darren, W. Buguo, High conductance in ultrathin films of ZnO, *Jpn. J. Appl. Phys.* 53 (2014) 05FJ01.
- J. Barbé, M.L. Tietze, M. Neophytou, B. Murali, E. Alarousu, A.E. Labban, M. Abulikemu, W. Yue, O.F. Mohammed, I. McCulloch, A. Amassian, S. Del Gobbo, Amorphous tin oxide as a low-temperature-processed electron-transport layer for organic and hybrid perovskite solar cells, *ACS Appl. Mater. Inter* 9 (2017) 11828–11836.
- A.K. Jena, M. Ikegami, T. Miyasaka, Severe morphological deformation of spiro-OMeTAD in (CH<sub>3</sub>NH<sub>3</sub>)PbI<sub>3</sub> solar cells at high temperature, *ACS Energy Letters* (2017) 1760–1761.
- C. Laura, K. Samrana, G. Michael, A. Shahzada, Hole-transport materials for perovskite solar cells, *Angew. Chem. Int. Ed.* 55 (2016) 14522–14545.
- C. Yu-Chieh, L. Kun-Mu, L. Chia-Hsin, L. Ching-Yuan, Direct C–H arylation meets perovskite solar cells: tin-free synthesis shortcut to high-performance hole-transporting materials, *Chem. Asian J.* 13 (2018) 1510–1515.
- X. Zhang, M. Li, C. Dall'Agnese, G. Chen, X.-F. Wang, T. Miyasaka, Thermo-evaporated pentacene and perylene as hole transport materials for perovskite solar cells, *Dyes Pigments* 160 (2019) 285–291.
- S. Ameen, M.A. Rub, S.A. Kosa, K.A. Alamry, M.S. Akhtar, H.-S. Shin, H.-K. Seo, A.M. Asiri, M.K. Nazeeruddin, Perovskite solar cells: influence of hole transporting materials on, *Power Conversion Efficiency* 9 (2016) 10–27.
- H. Xue, E. Birgersson, R. Stangl, Correlating variability of modeling parameters with photovoltaic performance: Monte Carlo simulation of a meso-structured perovskite solar cell, *Appl. Energy* 237 (2019) 131–144.
- H. Zhou, Q. Chen, G. Li, S. Luo, T.-b. Song, H.-S. Duan, Z. Hong, J. You, Y. Liu, Y. Yang, Interface engineering of highly efficient perovskite solar cells, *Science* 345 (2014) 542–546.
- M. Cha, P. Da, J. Wang, W. Wang, Z. Chen, F. Xiu, G. Zheng, Z.-S. Wang, Enhancing perovskite solar cell performance by interface engineering using CH<sub>3</sub>NH<sub>3</sub>PbBr<sub>0.912</sub> quantum dots, *J. Am. Chem. Soc.* 138 (2016) 8581–8587.
- D. Yang, X. Zhou, R. Yang, Z. Yang, W. Yu, X. Wang, C. Li, S. Liu, R.P.H. Chang, Surface optimization to eliminate hysteresis for record efficiency planar perovskite solar cells, *Energy Environ. Sci.* 9 (2016) 3071–3078.
- R. Lindblad, D. Bi, B.-w. Park, J. Oscarsson, M. Gorgoi, H. Siegbahn, M. Odelius, E.M.J. Johansson, H. Rensmo, Electronic structure of TiO<sub>2</sub>/CH<sub>3</sub>NH<sub>3</sub>PbI<sub>3</sub> perovskite solar cell interfaces, *J. Phys. Chem. Lett.* 5 (2014) 648–653.
- M.-C. Wu, Y.-H. Chang, Perovskite-Structured photovoltaic materials, in: B. Zaidi (Ed.), *Solar Panels and Photovoltaic Materials*, IntechOpen, 2018.
- M.F. Mohamad Noh, C.H. Teh, R. Daik, E.L. Lim, C.C. Yap, M.A. Ibrahim, N. Ahmad Ludin, A.R.B. Mohd Yusoff, J. Jang, M.A. Mat Teridi, The architecture of the electron transport layer for a perovskite solar cell, *J. Mater. Chem. C* 6 (2018) 682–712.
- M.-C. Wu, S.-H. Chan, K.-M. Lee, S.-H. Chen, M.-H. Jao, Y.-F. Chen, W.-F. Su, Enhancing the efficiency of perovskite solar cells using mesoscopic zinc-doped TiO<sub>2</sub> as the electron extraction layer through band alignment, *J. Mater. Chem.* 6 (2018) 16920–16931.
- S.-H. Chen, S.-H. Chan, Y.-T. Lin, M.-C. Wu, Enhanced power conversion efficiency of perovskite solar cells based on mesoscopic Ag-doped TiO<sub>2</sub> electron transport layer, *Appl. Surf. Sci.* 469 (2019) 18–26.
- Y. Sanehira, Y. Numata, M. Ikegami, T. Miyasaka, Spontaneous synthesis of highly crystalline TiO<sub>2</sub> compact/mesoporous stacked films by a low-temperature steam-annealing method for efficient perovskite solar cells, *ACS Appl. Mater. Interfaces* 10 (2018) 17195–17202.
- A. Kogo, Y. Sanehira, Y. Numata, M. Ikegami, T. Miyasaka, Amorphous metal oxide blocking layers for highly efficient low-temperature brookite TiO<sub>2</sub>-based perovskite solar cells, *ACS Appl. Mater. Interfaces* 10 (2018) 2224–2229.
- F. Di Giacomo, V. Zardetto, A. D'Epifanio, S. Pescetelli, F. Matteocci, S. Razza, A. Di Carlo, S. Licocchia, W.M.M. Kessels, M. Creatore, T.M. Brown, Flexible Perovskite Photovoltaic Modules and Solar Cells Based on Atomic Layer Deposited Compact Layers and UV-Irradiated TiO<sub>2</sub> Scaffolds on Plastic Substrates vol. 5, (2015), p. 1401808.
- J.P. Correa Baena, L. Steier, W. Tress, M. Saliba, S. Neutzner, T. Matsui,

- F. Giordano, T.J. Jacobsson, A.R. Srimath Kandada, S.M. Zakeeruddin, A. Petrozza, A. Abate, M.K. Nazeeruddin, M. Grätzel, A. Hagfeldt, Highly efficient planar perovskite solar cells through band alignment engineering, *Energy Environ. Sci.* 8 (2015) 2928–2934.
- [35] M.-C. Wu, Y.-H. Liao, S.-H. Chan, C.-F. Lu, W.-F. Su, Enhancing organolead halide perovskite solar cells performance through interfacial engineering using Ag-doped TiO<sub>2</sub> hole blocking layer, *Solar RRL* 2 (2018) 1800072.
- [36] T. Supasai, N. Henjongchom, I.M. Tang, F. Deng, N. Rujisamphan, Compact nanostructured TiO<sub>2</sub> deposited by aerosol spray pyrolysis for the hole-blocking layer in a CH<sub>3</sub>NH<sub>3</sub>PbI<sub>3</sub> perovskite solar cell, *Sol. Energy* 136 (2016) 515–524.
- [37] H. Li, B. Zheng, Y. Xue, S. Liu, C. Gao, X. Liu, Spray deposited lanthanum doped TiO<sub>2</sub> compact layers as electron selective contact for perovskite solar cells, *Sol. Energy Mater. Sol. Cells* 168 (2017) 85–90.
- [38] D.G. Lee, M. Kim, B.J. Kim, D.H. Kim, S.M. Lee, M. Choi, S. Lee, H.S. Jung, Effect of TiO<sub>2</sub> particle size and layer thickness on mesoscopic perovskite solar cells, *Appl. Surf. Sci.* 477 (2019) 131–136.
- [39] G. Murugadoss, G. Mizuta, S. Tanaka, H. Nishino, T. Umeyama, H. Imahori, S. Ito, Double functions of porous TiO<sub>2</sub> electrodes on CH<sub>3</sub>NH<sub>3</sub>PbI<sub>3</sub> perovskite solar cells: enhancement of perovskite crystal transformation and prohibition of short circuiting, *Apl. Mater.* 2 (2014) 081511.
- [40] L. Zhu, J. Shi, D. Li, Q. Meng, Effect of Mesoporous TiO<sub>2</sub> Layer Thickness on the Cell Performance of Perovskite Solar Cells, (2015).
- [41] A. Kogo, Y. Sanehira, M. Ikegami, T. Miyasaka, Brookite TiO<sub>2</sub> as a low-temperature solution-processed mesoporous layer for hybrid perovskite solar cells, *J. Mater. Chem.* 3 (2015) 20952–20957.
- [42] F. Xie, J. Zhu, Y. Li, D. Shen, A. Abate, M. Wei, TiO<sub>2</sub>-B as an electron transporting material for highly efficient perovskite solar cells, *J. Power Sources* 415 (2019) 8–14.
- [43] B. Cai, D. Zhong, Z. Yang, B. Huang, S. Miao, W.-H. Zhang, J. Qiu, C. Li, An acid-free medium growth of rutile TiO<sub>2</sub> nanorods arrays and their application in perovskite solar cells, *J. Mater. Chem. C* 3 (2015) 729–733.
- [44] Y. Yang, K. Ri, A. Mei, L. Liu, M. Hu, T. Liu, X. Li, H. Han, The size effect of TiO<sub>2</sub> nanoparticles on a printable mesoscopic perovskite solar cell, *J. Mater. Chem.* 3 (2015) 9103–9107.
- [45] C.J. Barbé, F. Arendse, P. Comte, M. Jirousek, F. Lenzmann, V. Shklover, M. Grätzel, Nanocrystalline titanium oxide electrodes for photovoltaic applications, *J. Am. Ceram. Soc.* 80 (1997) 3157–3171.
- [46] C.-Y. Huang, Y.-C. Hsu, J.-G. Chen, V. Suryanarayanan, K.-M. Lee, K.-C. Ho, The effects of hydrothermal temperature and thickness of TiO<sub>2</sub> film on the performance of a dye-sensitized solar cell, *Sol. Energy Mater. Sol. Cells* 90 (2006) 2391–2397.
- [47] H.-S. Kim, N.-G. Park, Parameters affecting I–V hysteresis of CH<sub>3</sub>NH<sub>3</sub>PbI<sub>3</sub> perovskite solar cells: effects of perovskite crystal size and mesoporous TiO<sub>2</sub> layer, *J. Phys. Chem. Lett.* 5 (2014) 2927–2934.
- [48] P.W. Liang, C.Y. Liao, C.C. Chueh, F. Zuo, S.T. Williams, X.K. Xin, J. Lin, A.K.Y. Jen, Additive enhanced crystallization of solution-processed perovskite for highly efficient planar-heterojunction solar cells, *Adv. Mater.* 26 (2014) 3748–3754.
- [49] N.G. Park, J. van de Lagemaat, A.J. Frank, Comparison of dye-sensitized rutile- and anatase-based TiO<sub>2</sub> solar cells, *J. Phys. Chem. B* 104 (2000) 8989–8994.
- [50] F. Giordano, A. Abate, J.P. Correa Baena, M. Saliba, T. Matsui, S.H. Im, S.M. Zakeeruddin, M.K. Nazeeruddin, A. Hagfeldt, M. Graetzel, Enhanced electronic properties in mesoporous TiO<sub>2</sub> via lithium doping for high-efficiency perovskite solar cells, *Nat. Commun.* 7 (2016) 10379.
- [51] Z. Xiao, Q. Dong, C. Bi, Y. Shao, Y. Yuan, J. Huang, Solvent annealing of perovskite-induced crystal growth for photovoltaic-device efficiency enhancement, *Adv. Mater.* 26 (2014) 6503–6509.
- [52] D. Wang, M. Wright, N.K. Elumalai, A. Uddin, Stability of perovskite solar cells, *Sol. Energy Mater. Sol. Cells* 147 (2016) 255–275.